Journal of Vibration Engineering & Technologies (2025) 13:557
https://doi.org/10.1007/s42417-025-02139-3

ORIGINAL PAPER

# Novel Inverse Multi-Objective Optimization-Empowered Design of Microperforated Panels for Enhanced Low-Frequency Noise Mitigation

**Duo Zhang**[1] · **Yang Zhang**[3] · **Sichen Yuan**[4] · **Jiong Tang**[3] · **Zequn Wang**[5] · **Kai Zhou**[1,2]

Received: 17 June 2025 / Revised: 24 August 2025 / Accepted: 23 September 2025

## Abstract

**Purpose** The microperforated panels (MPPs) display excellent capacity in noise control applications owing to the high strength, simple design, and efficacy in low-frequency sound absorption. Traditionally, the development of MPPs has relied on a trial-and-error design approach. Although optimization-based methods have recently begun to be employed, these designs often overlook practical considerations, such as increased costs associated with adding MPP layers, which presents a gap to achieve the practical feasibility of MPP deployment. To address this issue, the study aims to develop an inverse multi-objective optimization-empowered framework for MPP design to enhance low-frequency noise mitigation while minimizing fabrication costs.

**Methods** Specifically, a finite element (FE) model is established to conduct the acoustic analysis of MPPs, followed by thorough experimental validation. A novel multi-objective particle swarm optimization algorithm (MOPSO) is then developed to cope with mixed-type design variables with interrelations inherent to the general MPP architecture. Using the high-fidelity FE model as a cornerstone, the MOPSO guides the inverse optimization analysis to yield multiple non-dominated solutions.

**Results** These solutions not only avoid the trap of local optima, but also allow for continuous screening to ensure engineering viability based on empirical judgment. The results clearly demonstrate the effectiveness of the proposed methodology.

**Conclusions** The MPPs designed in this study show great potential for mitigating low-frequency noise in buildings with acceptable fabrication cost, addressing noise issues arising from rapid urbanization and transportation development in metropolitan areas. Furthermore, the novel optimization strategy proposed in this study holds wide applicability for other sound absorption materials.

**Keywords** Microperforated Panels · Sound Absorption · Fabrication Cost · Multi-Objective Particle Swarm Optimization · Inverse Optimization Analysis · Low-Frequency Noise

✉ Kai Zhou
cee-kai.zhou@polyu.edu.hk

Duo Zhang
duo-dz.zhang@polyu.edu.hk

Yang Zhang
yang.3.zhang@uconn.edu

Sichen Yuan
sichen.yuan@ua.edu

Jiong Tang
jiong.tang@uconn.edu

Zequn Wang
zequnwang@uestc.edu.cn

[1] Department of Civil and Environmental Engineering, The Hong Kong Polytechnic University, Hong Kong, China

[2] Research Institute for Sustainable Urban Development (RISUD), The Hong Kong Polytechnic University, Hong Kong, China

[3] Department of Mechanical Engineering, University of Connecticut, Storrs, CT 06269, USA

[4] Department of Aerospace Engineering and Mechanics, The University of Alabama, Tuscaloosa, AL 35487, USA

[5] Department of Mechanical and Electrical Engineering, University of Electronic Science and Technology of China, Chengdu, China

## Introduction

Acoustic comfort is a critical concern for urban communities. Rapid urbanization and transportation development have led to severe noise pollution in building environments, especially for those close to busy roads and railways [1, 2]. Indoor noise pollution can originate from both indoor and outdoor sources and often has low-frequency characteristics, which indicating that the noise frequency is below 1600 Hz [3–5]. For instance, indoor noise generated and transmitted by passenger vehicles typically ranges around 1 kHz, while the frequencies between 500 Hz and 1 kHz are produced by heavy trucks [6]. Additionally, indoor noise can be induced by heating, ventilation, and air conditioning (HVAC) systems and propagated through ductwork [7]. The dominant octave band frequency of HVAC noise is even lower, below 400 Hz [8, 9]. This noise adversely affects people's lives and work [10, 11]. Long-term exposure to severe noise can lead to various physiological and psychological diseases [12–14]. Given these adverse impacts, it is important to mitigate indoor noise using effective sound absorbers.

Commercial sound absorption materials can be generally classified into porous sound absorption materials (PMs) and resonant sound absorption materials (RMs) [15]. PMs are widely used to reduce noise across a broad frequency range with high absorption coefficients through air flow resistances, and viscous and thermal losses [16]. However, they are less effective at low frequencies due to the long sound wavelengths [17, 18]. RMs mainly include Helmholtz resonators (HRs) [19] and membrane absorbers [20], which exhibit good absorption properties in low and narrow frequency ranges because of the strong internal resonance effect [21]. Membrane absorbers typically consist of mass blocks and a tensioned membrane [22]. However, the instability of mass blocks and membrane creep can result in poor robustness by creating uneven tension distribution and altering the resonator's target frequency, limiting the practical application of membrane resonators [23]. In contrast, HRs are more likely to be adopted in practice. For improved sound absorption performance and easier manufacturing, HRs have evolved into a new class of sound absorbers, known as perforated panels, which operate on the principle of Helmholtz resonance absorption [24]. By adjusting the perforation ratio, perforated panels and HRs are interchangeable [25]. However, ordinary perforated panels with large holes and high perforation ratios typically require combination with porous materials in the cavity due to their inherently low acoustic resistance. To address this issue, Dah-You Maa [26] proposed reducing the perforation diameter to enhance acoustic resistance, leading to the development of MPPs. Compared to ordinary perforated panels, MPPs offer a broader sound absorption band due to the viscous effect around the tiny, perforated holes [1, 27].

MPPs can be fabricated from any sheet material [28], which offers significant practical advantages. The flexibility in material choice allows for the use of low-cost, readily available materials or specific materials (e.g., lightweight polymer sheets, corrosion-resistant metals) depending on application requirements. Common industrial processes can be applied to diverse materials to simplify large-scale production and adoption. Compared with membrane absorbers that are also effective for low-frequency noise control, MPPs have been extensively applied to enhance the acoustic environment in various scenarios because of their low cost, high strength, and simple design [29]. MPPs must be installed in front of a rigid wall because their sound absorption performance becomes negligible without the air gap [30]. This strategic placement endows MPPs with substantial potential to address the indoor noise issues [1], allowing for the design adjustment to adapt to different room settings [31, 32]. Several successful cases of indoor noise mitigation using MPPs are shown in Fig. 1. Furthermore, MPPs can also be deployed over the front rotor of the contra-rotating fan [33], inside helicopter cabins [34], in wind tunnel test areas [35], in noise barriers [36], and in fighter cockpits [37].

Single-layer MPP is commonly used for noise reduction. However, it is limited in providing a broad frequency attenuation band compared to conventional porous materials [38]. Conversely, multi-layer MPP, comprising different air cavities for each layer, can extend the frequency attenuation band by enabling multiple absorption peaks [39]. For improving the structural stability and avoiding recycling hindrance, mechanically fastened layers (e.g., screw-bonded) are more likely to be adopted. However, adding layers also introduces additional air cavities, which increases the thickness of synthesized MPPs. This may lead to installation challenges in practical applications. Furthermore, the assembly process becomes more complex, and the associated costs can rise significantly. From a design standpoint, the design of a multi-layer MPP requires the examination of many influential structural parameters and their intrinsic intercorrelation, making it technically challenging. Historically, the MPP design based on the trial-and-error approach was indeed prevalent, which heavily relies on experience and judgment [40–44]. For a single-layer configuration, this approach might be feasible because of the limited number of structural parameters being investigated during the design process. However, due to the increasing complexity of the multi-layer MPP design mentioned above, the trial-and-error approach struggles to balance design accuracy with time efficiency [45].

With the advancement of computational power, computational design has emerged as an effective solution to

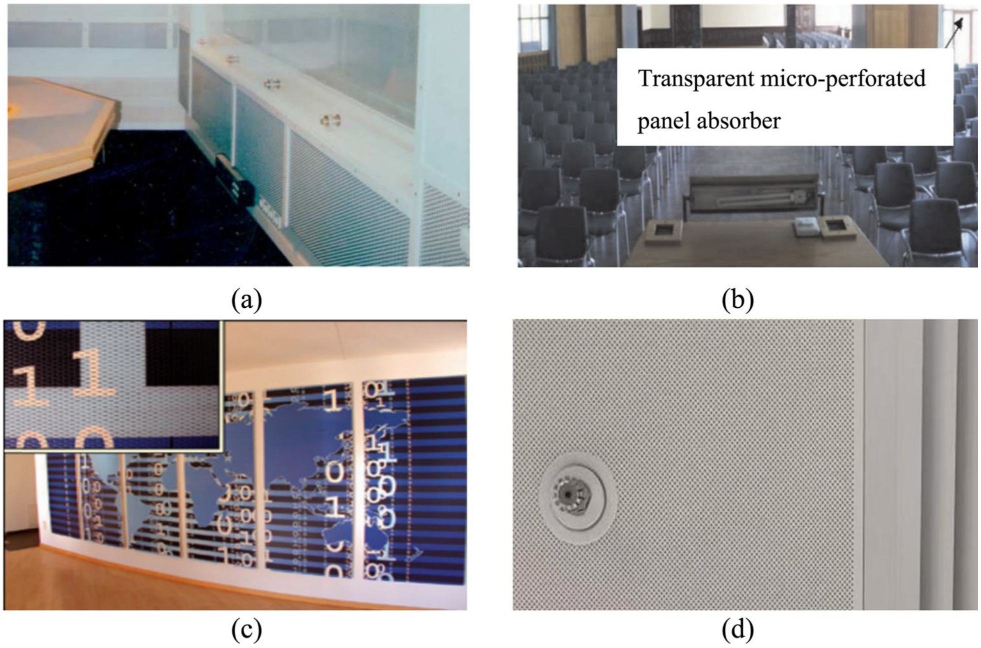
(a) (b) (c) (d)

**Fig. 1** Practical application scenarios of MPPs: (**a**) A speaker's studio at RTL, Köln, reprinted with permission from [46], copyright (2006) European Acoustics Association; (**b**) The assembly hall of the University of Freiburg, reprinted with permission from [47], copyright (2001) European Acoustics Association; (**c**) The reception area, reprinted with permission from [48], copyright (2011) Tech Science Press; and (**d**) The vent of Pao Yue-kong Library at PolyU

advance MPP development. In such computational design, the design problem is rigorously formulated as a mathematical problem, which is then solved through optimization analysis [49, 50]. Compared to the traditional trial-and-error design approach, its advantages are evident, such as implementation autonomy without manual interference, excellent capability of solution search, etc. Within this computational framework, previous studies have analytically calculated the function related to the normal sound absorption coefficient (SAC) and used it as the design optimization objective to guide the design analysis. Cobo et al. [51] applied a simulated annealing (SA) algorithm to optimize the parameters of triple-layer MPPs for the maximum mean absorption coefficient within a prescribed frequency band. Qian et al. [52] proposed a multi-population genetic algorithm (GA) to optimize the design of an MPP with varying hole sizes, aiming to maximize average absorption within a specified frequency band. Lu et al. [53] used the particle swarm optimization (PSO) algorithm to enhance the mean absorption of four distinct types of MPPs. Wang and Bennett [54] applied the sequential quadratic programming (SQP) algorithm to minimize the sound power reduction factor of an MPP featuring multiple chambers. In addition to the analytical derivation of the design optimization objective, FE simulation has also been adopted for its greater accuracy and applicability [55–57]. By comparison with analytical models, FE simulations account for detailed geometric features, material heterogeneities, and broader frequency-domain behavior, thereby offering more accurate predictions for general cases. Although the methods for evaluating the design optimization objective differ, the design implementation processes remain the same.

It is worth emphasizing that the state-of-the-art studies discussed above have primarily focused on examining a single design optimization objective, namely sound absorption performance. In recent years, researchers have sought to achieve a balance between sound absorption performance and other key metrics in panel absorbers. For instance, Li et al. [58] developed a double-layered irregular honeycomb MPP structure, optimizing its parameters for broadband and high-efficiency sound absorption. Similarly, Sheng et al. [59] designed a novel metamaterial, named quasi-periodic sonic black hole, to achieve both acoustic bandgap and elastic bandgap. Meanwhile, Jian et al. [60] introduced an optimization strategy for thickened triple periodic minimal surfaces to achieve simultaneous low-frequency noise suppression capabilities and excellent mechanical performance. While these studies successfully address acoustic and structural performance, they often overlook the practical cost implications of such designs. Actually, the structural parameters of multi-layer MPPs also significantly impact the absorber fabrication cost, particularly in terms of processing and materials. For multi-layer MPPs to be widely employed in buildings, their cost also needs to be minimized [57]. Moreover, multi-layer MPPs with different layers exhibit varying acoustic performances and assembly costs. Therefore, the number of layers should be considered an independent design variable in the optimization problem. Previous studies, on the other hand, have typically focused on MPPs with a fixed number of layers. Given this context, multi-objective design optimization with an expanded design space for multi-layer MPPs is essential for continuous advancements in sound absorption capacity and fabrication cost. Nevertheless, this approach presents a technical challenge from a mathematical optimization perspective. Specifically, the number of layers is a discrete variable, while the MPP parameters, such as the diameter of perforations, panel thickness, perforation ratio, and cavity depth, are continuous variables. Moreover, the total number of MPP parameters depends on the number of layers. This combination results in a constrained hybrid optimization problem involving multiple types of design variables. To our knowledge, such a design problem holds practical significance but has not yet been thoroughly investigated or solved. Addressing this knowledge gap represents a key motivation for our research and provides an opportunity for methodological innovation in optimization techniques.

This study aims to establish an integrated design framework to achieve effective MPP design with generic geometric configurations. This framework is built upon the seamless integration of numerical modeling, experimental investigation, and novel multi-objective optimization algorithm to simultaneously maximize sound absorption capacity and minimize fabrication cost. In-house codes are specifically developed for the multi-objective optimization algorithm, as well as for the integration and implementation of the framework. The entire manuscript is structured as follows: Sect. 1 presents the background of the study. Section 2 establishes the FE model used to conduct the acoustic analysis of the MPP, followed by comprehensive experimental validation. Section 3 formulates the design optimization problem and introduces the proposed multi-objective optimization algorithm to facilitate the multi-layer MPP design. Section 4 draws conclusions and offers future prospects.

## Numerical Modeling with Experimental Validation

### Acoustic Analysis of MPPs

As illustrated in Fig. 2, the general configuration of the MPP is defined by its geometric parameters, including the diameter of the perforation (i.e., $d$), the panel thickness (i.e., $t$), and the cavity depth (i.e., $D$). For a cylindrical MPP with radius $R_p$ and $M$ circle holes uniformly distributed over the panel, the perforation ratio $\sigma$, defined as the ratio of perforations' area to the total surface area of the panel, can be calculated as

$$\sigma = \frac{Md^2}{4R_p^2} \tag{1}$$

After specifying the above geometric parameters, the numerical model can be established through the FE method, and the acoustic analysis can then be performed. As illustrated in Fig. 3, the model typically consists of three subdomains, including perfectly matched layer (PML), waveguide, and

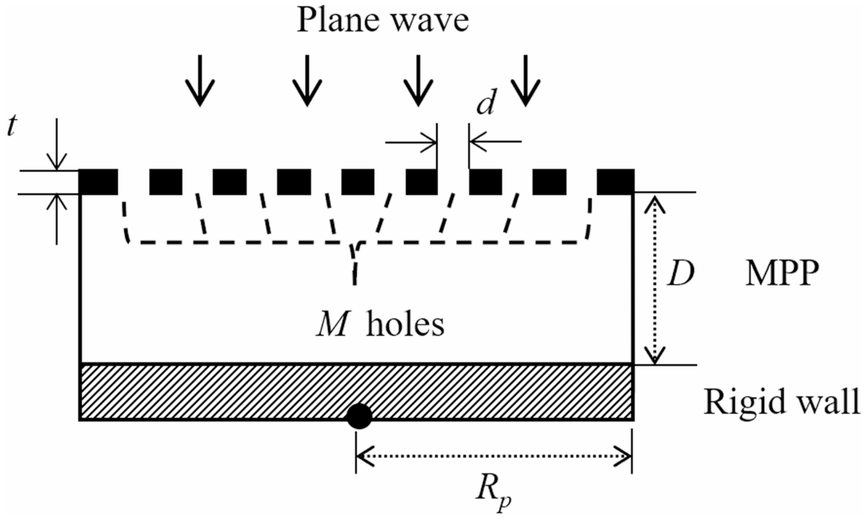

**Fig. 2** Illustration of the general MPP configuration

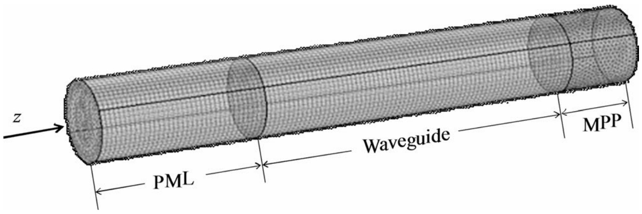

**Fig. 3** Description of FEM model domains

MPP subdomains, intending to elucidate the sound wave propagation characteristics. Specifically, PML in this model is imposed to absorb outgoing waves from the waveguide subdomain. The waveguide and MPP subdomains are backed by the hard/rigid walls. The sound propagation in the frequency domain is characterized by the Helmholtz equation as

$$\nabla \cdot \left(-\frac{1}{\rho}\nabla p\right) - \frac{p\omega^2}{\rho c^2} = 0 \tag{2}$$

where $\rho$ denotes the air density, $p$ denotes the sound pressure, $\omega$ denotes the angular frequency of sound wave, and $c$ denotes the sound speed in the air. By solving Eq. (2), the total acoustic pressure can be expressed as

$$p_t = p_i + p_r \tag{3}$$

where $p_i$ and $p_r$ denote the incident and reflected acoustic pressure, respectively. When the sound wave is injected along the z-coordinate axis, $p_i$ can be derived as

$$p_i = p_0 exp(-j\boldsymbol{k} \cdot \boldsymbol{z}) \tag{4}$$

where $p_0$ denotes the wave amplitude, $\boldsymbol{k}$ denotes the wave vector defined by the wave number, and $\boldsymbol{z}$ represents the location on the interior boundary. When the sound wave passes through an interior boundary, the acoustic pressure loss can be described as

$$\Delta p_t = Z_t \cdot v_n \tag{5}$$

where $Z_t$ represents the transfer impedance of an interior boundary given a medium or material, and $v_n$ represents the normal acoustic velocity. Here, transfer impedance measures the ability of a boundary or structure to transmit sound energy from one side to the other. This is a key parameter for describing the sound wave propagation behavior through a medium or material and should therefore be considered in acoustic analysis.

The transfer impedance of the MPP is influenced by several factors, including the transfer impedance of holes, end correction, hole-hole interaction, nonlinear effects, and resonance of air cavity. Because the panel is very thin, its energy losses due to heat conduction are negligible. As shown in Fig. 4**(a)**, we assume the sound wave is injected along the z-coordinate axis perpendicular to the panel. The acoustic pressure and the sound velocity along the $z$-axis are.

$p(z) = pexp(-jk_c z), \boldsymbol{v}(z) = \boldsymbol{v}exp(-jk_c z)$ (6a, b).

where $k_c$ denotes the complex wave number. Substituting Eqs. (6a, b) into Eq. (5) leads to

$$Z_n = \frac{p(z+t) - p(z)}{v_n(z+t/2)} = -2jZ_c \sin\frac{k_c t}{2} \tag{7}$$

where $Z_n$ represents the transfer impedance of a hole, and $Z_c$ represents the characteristic impedance, which is the product of the density of the medium and the speed of sound within it. Since thermal effects are negligible for thin panel, the normalized transfer impedance of a hole can be expressed based on Eq. (7) as follows [61]:

$$z'_n = \frac{Z_n}{\rho c} = -\frac{j\omega}{c}\frac{t}{\gamma_v} \tag{8}$$

where $\gamma_v$ denotes the mean value of the scalar viscous function at the cross section. The scalar viscous function typically represents viscosity at a given point in the fluid. Consequently, the normalized transfer impedance of all the holes is described as

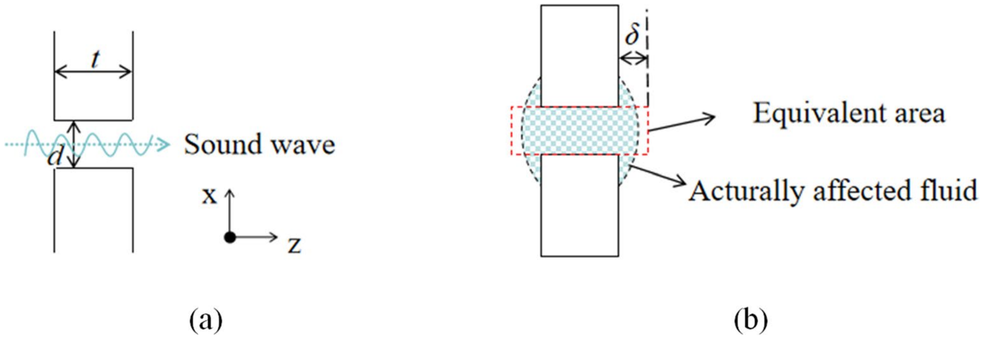

(a) (b)

**Fig. 4** Propagation of sound waves: (**a**) Direction of sound waves; (**b**) Rationale behind end correction

$$z_p = \frac{{z_n}'}{\sigma\, C_D} \tag{9}$$

where $C_D$ represents the ratio of the actual flow rate of a fluid through a hole to the theoretical flow rate under ideal conditions.

It should be noted that Eq. (9) only considers the fluid within the holes. However, the incident wave affects more fluid around the hole. The equivalent area is longer than the panel thickness by $\delta$ on each side, as shown in Fig. 4 **(b)**. Therefore, Eq. (9) should be modified to account for end corrections for the equivalent area of the fluid. The hole-hole interaction can be evaluated by a factor $f_{int}$, the so-called *Fok function*, which is expressed by

$$f_{int} = \sum {}_{n=0}^{8} a_n \left(\sqrt{\sigma}\right)^n \tag{10}$$

where $a_n$ denotes the multinomial coefficients. The selection of the values is referred to [62]. Hence, the end correction and hole-hole interaction can be further expressed as

$$z_{end} = -\mathrm{Re}\left(\frac{j\omega}{c\sigma\, C_D}\frac{2\delta}{\gamma_v} f_{int}\right) - j\mathrm{Im}\left(\frac{j\omega}{c\sigma\, C_D}\frac{2\delta}{\gamma_v} f_{int}\right) \tag{11}$$

Moreover, the normalized transfer impedance of the back air cavity can be calculated as [63, 64]

$$z_{air} = -j\cot(k_c \cdot D) \tag{12}$$

Combining Eqs. (8)-(12), the normalized transfer impedance of the MPP can be derived as

$$\begin{aligned} z_t = {} & -\mathrm{Re}\left(\tfrac{j\omega}{c\sigma\, C_D}\tfrac{t+2\delta}{\gamma_v} f_{int}\right) \\ & -j\mathrm{Im}\left(\tfrac{j\omega}{c\sigma\, C_D}\tfrac{t+2\delta}{\gamma_v} f_{int}\right) - j\cot(k_c \cdot D) \end{aligned} \tag{13}$$

where $z_t$ denotes the normalized transfer impedance of the MPP. On this basis, the SAC, which represents sound absorption capacity of the MPP, is derived as [63–65]

$$\alpha = 1 - \left|\frac{z_t - 1}{z_t + 1}\right|^2 \tag{14}$$

where $\alpha$ denotes the SAC. As can be seen from the above formulation, the SAC is essentially a function of geometric parameters depicted in Fig. 2. As an important measure of acoustic performance, it will be used as the design optimization objective to guide the MPP design, as will be introduced in Sect. 3.1.

To implement the fundamental principle outlined above, we utilize *COMSOL Multiphysics* to build the FE model and conduct the acoustic analysis. The aluminum is specifically chosen for the MPP, including both the panel and cavity, according to its wide use [66, 67] and inherent incombustibility [68, 69]. The perfectly matched layer (PML) and waveguide subdomains are discretized by swept meshing, while tetrahedral elements are employed for the MPP subdomain. The sizes of all elements are set below one-sixth of the minimum wavelength of the incident sound wave to ensure the desired simulation accuracy. The entire computational domain in FE model consists of over 44,000 degrees of freedom (DOFs). A single FE simulation run takes approximately 2 min to complete on a computer with an i5-8400 CPU, 4 GB of RAM memory, and the Windows 10 Home operating system.

## Experimental Correlation Analysis

To validate the accuracy of the FE model established in Sect. 2.1, an experimental investigation is conducted. Specifically, two MPP specimens with varying perforation ratios and cavity depths (as shown in Fig. 5) are fabricated, in which the MPP panels are perforated using the electrical discharge machining (EDM). We have implemented stringent quality control measures during fabrication, including microscopic examination of sample holes to ensure they closely approximate the designed cylindrical geometry. The panel thickness and perforation diameter of both specimens are 0.35 mm and 0.25 mm respectively. The short MPP, with a cavity of 6 cm, has a perforation ratio of 0.75%, while the tall MPP, with a cavity of 9 cm, has a perforation ratio of 0.9%. It is noted that several practical considerations inform our specimen selection strategy. First, our choices are constrained by both the physical size limitations of our impedance testing equipment and the need for precise, repeatable measurements. Such requirement can be easily and reliably satisfied by single-layer MPP configurations. Although the testing on multi-layer MPP configurations could potentially offer more comprehensive benchmarks, these configurations introduce greater installation sensitivity and higher susceptibility to measurement errors. We conduct impedance tube testing on the two selected specimens with the geometric parameters described above.

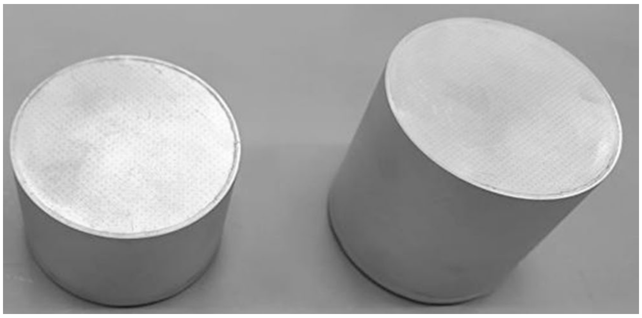

**Fig. 5** Two MPP testing specimens

In this test, a two-microphone impedance tube (*Brüel & Kjær Impedance Tube Kit Type 4206*) following the *ISO 10534-2* and *ASTM E1050-12* standards is utilized to measure SAC of specimens. Since few indoor noise sources exhibit significant levels above 1600 Hz that pose a substantial concern in residential areas [70], we focus on the sound absorption performance of MPPs below 1600 Hz. Therefore, we use a 100 mm diameter tube of Type 4206, which can measure frequencies from 50 Hz to 1600 Hz, and design the external diameter of specimens accordingly for installation (see Fig. 5). Before testing, microphone calibration is conducted to ensure the reliability and accuracy of the results [71, 72]. The tests with porous absorbers are carried out as the benchmark. Since the dominant source of measurement uncertainty in the sound pressure level stems from the microphone calibration uncertainty at the ultrasound frequency (55.5 kHz), the results remain reliable across the target frequency range [73]. After gently inserting the sample into the tube, installers applied a continuous ring of Blu-tack adhesive putty around the sample perimeter to ensure airtight installation. A final inspection verifies a perfect fit without visible indentations. A loudspeaker at one end of the tube generates broadband stationary random sound waves, and two microphones measure the resulting sound pressure. In alignment with our focus on typical indoor noise conditions, all experimental measurements are conducted using an incident sound pressure level of 90 dB, representative of common low-level acoustic environments. At this moderate excitation level, nonlinear acoustic effects are negligible, ensuring the SAC remains independent of incident sound pressure level [74]. The SAC of specimens is derived based on *ISO 10534-2* and *ASTM E1050-12* methods. Each specimen is tested three times to minimize the adverse effect of uncertainties, and the recorded values are averaged. The test equipment layout is shown in Fig. 6.

The performance of the MPPs for these two specimens has been further analyzed. The results, shown in Fig. 7, compare the experimental data (blue line) with the numerical results (red line). As shown, the specimen in Fig. 7b outperforms that in Fig. 7a within the frequency range below approximately 700 Hz. Conversely, as the target frequency increases, the specimen in Fig. 7a exhibits a relatively slower decrease beyond 700 Hz. The frequency ranges corresponding to the absorption peaks show slight shifts between these two specimens. However, more pronounced frequency shifts for absorption peaks are expected among the design candidates under combinatory design in high-dimensional space. The notable discrepancies of the specimens in performance, as shown in Fig. 7, emphasize the necessity of optimizing MPP design across the entire target frequency range. These results also illustrate the proper selection of specimens, enabling comprehensive validation of the numerical model.

Interestingly, sound absorption valleys are observed in the experimental results. This phenomenon is primarily due to panel vibrations that compromise absorption performance at the structural resonant frequency [75, 76]. This complex effect is not evident in numerical results, as the panel is considered ideally rigid in the FE model to reduce computational complexity and thus facilitate FE-based inverse optimization analysis. To quantitatively assess the significance of the observed valleys in the experimental results, we define an evaluation function to compute the average acoustic performance within specified frequency ranges [55]

$$Q_{\Omega}\left(f_1, f_2\right) = \int_{f_1}^{f_2} \alpha_{\Omega}\left(f\right) \approx \sum{}_{f_1}^{f_2} \alpha_{\Omega}\left(f\right) \tag{15}$$

where $f_1$ and $f_2$ represent the lower and upper frequency bounds, respectively, $\alpha_{\Omega}\left(f\right)$ denotes the SAC value

**Fig. 6** The impedance tube test: (**a**) Instrumentation setup; (**b**) The specimen inside the tube

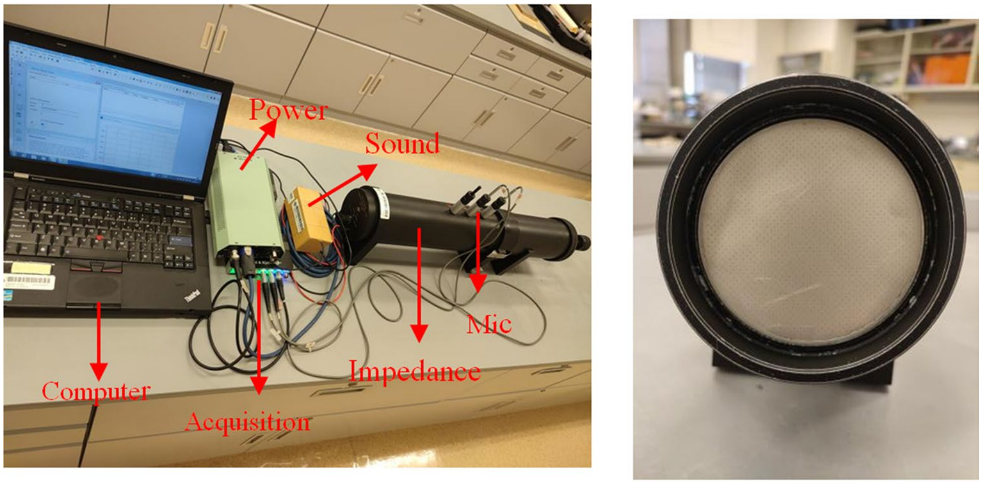

(a) (b)

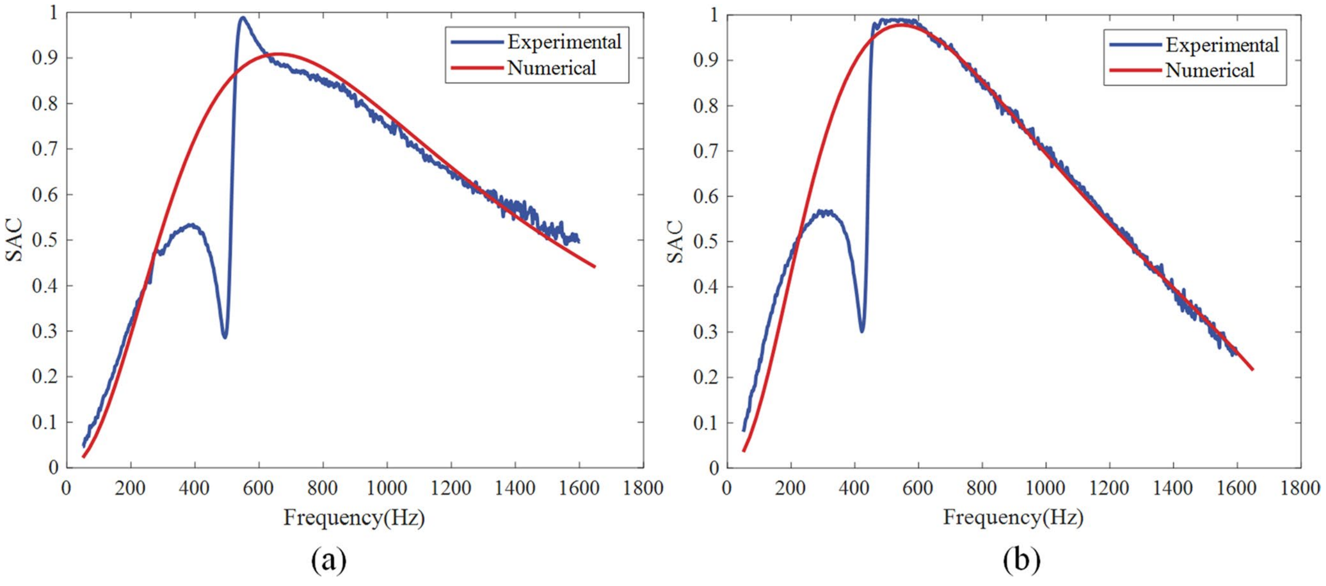

**Fig. 7** Comparison of experiment and numerical results for MPPs with a thickness of 0.35 mm and perforation diameter of 0.25 mm: (a) $\sigma$ =0.75%, $D$=6 cm; (b) $\sigma$ =0.9%, $D$=9 cm

at a certain frequency $f$, and $\Omega$=1 and $\Omega$=2 correspond to experimental and numerical results, respectively. Applying this metric to Fig. 7(a), the relative magnitude of the valley between 270 Hz and 530 Hz is calculated as: $\frac{Q_2(270{,}530)-Q_1(270{,}530)}{Q_2(50{,}1600)}=0.054$. Similarly, for Fig. 7(b), the valley between 230 Hz and 450 Hz yields: $\frac{Q_2(230{,}450)-Q_1(230{,}450)}{Q_2(50{,}1600)}=0.058$. These results demonstrate two key findings: (1) The valley magnitudes are relatively small (5.4% and 5.8% of the overall performance); (2) The valley characteristics show remarkable consistency between different cases. In general, the numerical results overall align with the experimental results, except for the presence of the sound absorption valley, indicating the capability of the FE model to capture the underlying acoustic characteristics of actual MPPs. The comparison of results verifies the FE model accuracy, laying the foundation for subsequent MPP design optimization.

## Design Optimization Implementation

### Problem Formulation

As introduced in Sect. 2.1, the SAC of the MPP depends on its geometric parameters denoted as ($d$, $t$,$\sigma$, $D$). For an MPP with $i$ layers, as shown in Fig. 8, its geometric parameters can be generally represented by the vector of ($d_1$, $t_1$,$\sigma_1$, $D_1$, $d_2$, $t_2$,$\sigma_2$, $D_2$,…, $d_i$, $t_i$,$\sigma_i$, $D_i$). Increasing the number of layers, i.e., $i$, will certainly expand the design optimization space, therefore compounding the complexity of optimization analysis. As a special case, the multi-layer MPP converts into a single-layer MPP when $i$ is set to 1.

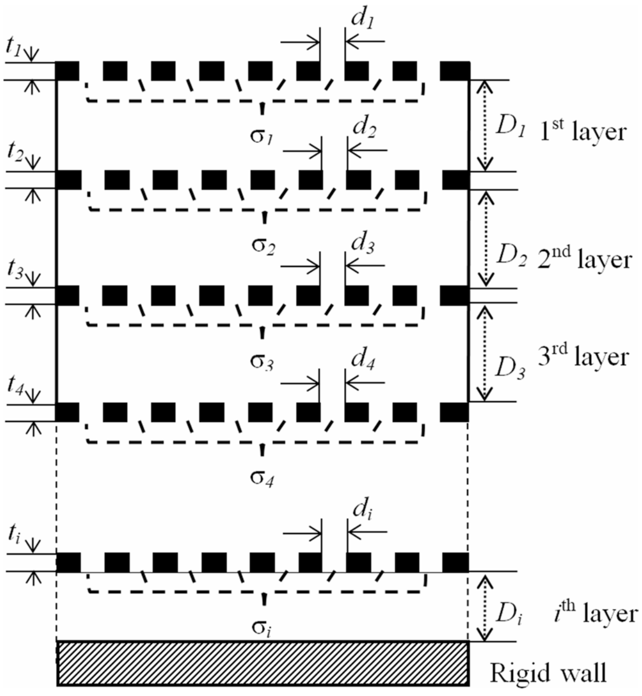

**Fig. 8** Illustration of the generic MPP configuration and related design variables

The effectiveness of MPP is primarily measured by its sound absorption performance. As mentioned in the Introduction, low-frequency noise is the major component of indoor noise that disrupts residents. Therefore, this research focuses on enhancing absorption performance below 1600 Hz, aligning with the impedance tube testing capacity described in Sect. 2.2. Without bias towards specific frequency components, we formulated a metric to evaluate the overall absorption performance of the MPP by integrating the SAC curve over the target frequency range of 50–1600 Hz, based on Eq. (15).

$$S = \int_{50}^{1600} \alpha\ (f) \approx \sum{}_{50}^{1600} \alpha\ (f) \tag{16}$$

SAC curve here can be evaluated through FE simulation given the MPP configuration. This performance indicator can be written as an implicit function of geometry parameters:

$$S = \vartheta\ (d1,\ t1, \sigma\ 1,\ D1,\ d2,\ t2, \sigma\ 2,\ D2, ...,\ di,\ ti, \sigma\ i,\ Di) \tag{17}$$

where $\vartheta$ indicates the operation involving the FE simulation and SAC curve integration.

For practical deployment in building environments, the fabrication cost of the MPP from an economic perspective should also be considered. In this research, the fabrication cost of the MPP is defined as the sum of material and processing costs. Recall that a typical MPP consists of layers of panels backed with respective air cavity, and a rigid wall, as illustrated in Fig. 8. Since MPPs are usually placed in front of walls or beneath ceilings [1], there is no need to specially fabricate the rigid wall. For MPPs applied over a wide area, the fabrication cost of the cavity is often much less than that of the panels. Therefore, the fabrication cost of the MPP is mainly covered by the cost of the panels, which can be simply estimated as

$$C_f = C_m + C_p \tag{18}$$

where $C_f$, $C_m$, and $C_p$ represent the fabrication, material, and processing costs of the panels included in the MPP, respectively. The total cost of materials used for fabricating panels can be calculated as

$$C_m = \sum{}_i A \cdot t_i \cdot \rho_{\ m} \cdot P_m \tag{19}$$

where $A$ denotes the panel surface area, which is typically the same for all panels. $t_i$ is the thickness of the $i$-th panel, $\rho_{\ m}$ is the density, and $P_m$ is the unit price of the panel material.

Based on empirical knowledge, the processing cost of panels is approximately proportional to the number of holes in them, as expressed by the following equation:

$$C_p = \sum{}_i M_i \cdot P_h \tag{20}$$

where $M_i$ is the hole number of the $i$-th panel, which can be derived based on the respective perforation ratio defined in Eq. (1). $P_h$ denotes the unit price of perforating a hole by EDM method.

With the full definition of costs in relation to materials and processing (Eqs. (19) and (20)), the total fabrication cost of the MPP outlined in Eq. (18) can be evaluated. Given that aluminum is primarily used for the panels, its material properties and unit price are well-documented. Specifically, the density of aluminum, i.e., $\rho_{\ m}$ in Eq. (19) is set at $2.7 \times 10^3$ kg/m³, and the unit price, i.e., $P_m$ is approximately 20 HKD/kg. The surface area of the panel, i.e., $A$ in Eq. (19) is consistently set at 1 $m^2$. Moreover, the price for processing a single hole, i.e., $P_h$ in Eq. (20) is approximately 0.04 HKD based on the consultation from the manufacturing company. Although the unit prices used may not be entirely precise, they do not impact on the optimization results as they remain constant. We select as reasonable price values as possible to ensure the actual costs are easy to interpret in the succeeding result discussion. While the cost metric employed in this study represents a simplified formulation that may not account for all practical manufacturing considerations (due to limited industry consultation), this simplification does not affect the validity of our methodology. It should also be noted that the proposed framework is designed to accommodate more comprehensive cost formulations when additional fabrication expertise and detailed production data become available. By substituting all constants into the Eqs. (19) and (20), the Eq. (18) can be rewritten as

$$C_f = \sum{}_i [5.4 \times\ 10^4 t_i + \frac{0.16\sigma\ _i}{\pi\, d_i^{\ 2}}] \tag{21}$$

Both design objectives, expressed in Eqs. (17) and (21), are fundamentally linked through their shared dependence on the key geometric parameters of ($d$, $t$,$\sigma$, $D$). Therefore, these parameters can be considered as design variables in the subsequent design optimization. It is well known that these parameters should fall within a certain range to well serve the purpose of practical implementation. For example, the panel of the MPP is ultra-thin, usually no more than 1 mm in thickness [1, 26]. The hole diameters are typically no more than 1 mm [77]. Due to the reduced accuracy of the EDM method for manufacturing very small holes, we have set the lower bound of the hole diameter at 0.2 mm. Typically, the perforation ratio of the MPPs is under 2% [1, 27, 43]. The total cavity depth depends on the specific installation environment. In this study, we assume that the total thickness of the MPP should not exceed 9 cm, with the total cavity depth playing a dominant role. Based on the above set of constraints, the multi-objective optimization problem, specifically a bi-objective optimization problem involving the design objectives shown in Eqs. (17) and (21), is formulated as follows:

$$\begin{cases} Maximize\, S(x) \\ Minimize\, C_f(x) \\ x = [d_1,\, t_1,\, \sigma_1,\, D_1,\, d_2,\, t_2,\, \sigma_2,\, D_2,\, \ldots,\, d_i, t_i,\, \sigma_i,\, D_i, i] \end{cases}$$

Subject to

$$\begin{aligned} & 0.0002 \leq d_i \leq 0.001\,\mathrm{m},\ i \in N^* \\ & 0.0001 \leq t_i \leq 0.001\,\mathrm{m},\ i \in N^* \\ & 0.002 \leq \sigma_i \leq 0.02,\ i \in N^* \\ & D_i > 0,\ i \in N^* \\ & \sum{}_i D_i + t_i \leq 0.09\,\mathrm{m},\ i \in N^* \end{aligned} \tag{22}$$

.

where $N^*$ is the maximum number of layers in the MPP. Although the proposed MOPSO algorithm can theoretically optimize models with an unlimited number of layers (i.e., the upper limit approaches infinity), each additional layer introduces four new structural parameters, significantly increasing computational complexity and runtime. To balance efficiency with demonstration needs, we implement a three-layer configuration as a representative case, ensuring both computational feasibility and effective validation of the model and algorithm. To facilitate the optimization, the negative $S(\boldsymbol{x})$ will be used to convert the problem into a minimization problem.

## Multi-objective Particle Swarm Optimization (MOPSO) Algorithm and Integrated Design Framework

According to the problem described in Eq. (22), the number of layers in the MPP is essentially a discrete variable denoted by *i*. This discrete variable dynamically influences the number of continuous design variables, as each layer contains four geometric parameters treated as continuous values. Consequently, changes in the number of layers lead to corresponding changes in the number of design variables. The challenge lies in managing both the hybrid nature of variables (discrete and continuous) and dynamic adjustments to these variables during the optimization process. While the conventional Non-dominated Sorting Genetic Algorithm can theoretically solve this multi-objective optimization problem, it faces significant limitations in computational efficiency when handling the mixed-type design variables and their dynamic interrelations inherent to our MPP design framework [78, 79]. To address these issues, we develop an alternating optimization algorithm on the basis of the MOPSO, to solve the multi-objective optimization problem formulated in Eq. (22), while obtaining a set of trade-off solutions. Among the various optimizers, MOPSO is selected due to its rapid convergence and generation of a range of trade-off solutions in a single run. Additionally, MOPSO allows for the development of local search strategies that can further refine the search process. PSO algorithm is a stochastic technique first introduced by Eberhart and Kennedy [80]. It models the social behavior of animals such as insects, herds, birds, and fish. In this cooperative approach, each member of the bird adjusts its search pattern based on both its own learning experiences and those of other members.

The search process of the PSO is illustrated in Fig. 9. In this process, each particle moves towards its personal best position stored in its memory and the global best position among all particles. Mathematically, the new velocity and position of each particle can be expressed as Eqs. (23) and (24):

$$v_j(t+1) = wv_j(t) + c_1 r_1 (p_{best}(t) - x_j(t)) + c_2 r_2 (g_{best}(t) - x_j(t)) \tag{23}$$

$$x_j(t+1) = x_j(t) + v_j(t+1) \tag{24}$$

where *v* is the velocity of the particle, *x* is the position of particle or the solution of the optimization problem, $r_1$ and $r_2$ are random numbers, *t* is the current iteration, $p_{\mathrm{best}}$ is the personal best, and $g_{\mathrm{best}}$ is the global best. In the above equations, coefficient *w* is the inertia weight, $c_1$ is the coefficient of the cognitive component which indicates that each particle learns from its experience, and $c_2$ is the coefficient of the social component, from which all particles learn. Although PSO is widely used in various applications [81–83], conventional single-loop optimization methods struggle to efficiently handle mixed variable types in MPP design. To address this challenge, we adapt the conventional MOPSO by incorporating an alternative loop over the discrete variables, separating the optimization process into nested

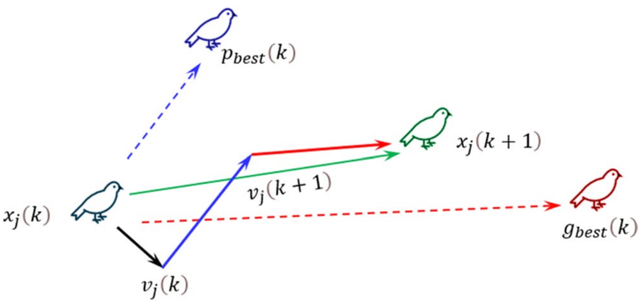

**Fig. 9** Illustration of the particle swarm-based search

loops. This approach allows us to systematically explore the performance-cost landscape and identify optimal balance points. Moreover, we use the hypervolume indicator to evaluate algorithm performance and drive iteration. The hypervolume is a metric in multi-objective optimization that measures the volume of objective space dominated by a solution set, relative to a chosen reference point [84]. This indicator provides a comprehensive measure that accounts for both convergence and diversity of solutions in our bi-objective space (performance and cost). The reference point for hypervolume calculation is set at 1.1 times the nadir point (the point with the worst values across all objectives) to ensure all Pareto optimal solutions contribute positively to the evaluation. The entire logic flow of the optimizer proposed is shown in Fig. 10.

Specifically, the algorithm operates by iterating over different discrete variable values *N*. The discrete variable *N* represents the number of MPP layers in the acoustic isolation system. While increasing *N* generally enhances acoustic performance, it may lead to higher manufacturing costs, creating a fundamental trade-off that our optimization framework addresses. For each discrete variable value, a set of particles (solutions) is initialized, where each particle has 4, 8, or 4*N* continuous variables, depending on the chosen discrete variable (layers of MPP). The continuous variables represent the physical parameters of each MPP layer, including perforation diameter, perforation ratio, panel thickness, and cavity depth, as marked in Fig. 8. These parameters directly affect the SAC across different frequency bands, especially in the low-frequency range. Our multi-objective function simultaneously evaluates two competing criteria introduced above. The adapted MOPSO is then applied, allowing particles to move within the search space while updating their positions and velocities using Eqs. (23)-(24). Each particle's objective function values are evaluated, and non-dominated solutions are stored in an archive. After each MOPSO run, the hypervolume of the current Pareto front is calculated. If the hypervolume improves, the corresponding discrete variable value and Pareto front are saved. This process is repeated multiple times to identify the optimal discrete variable value. Finally, the best discrete variable value and the corresponding Pareto front are returned. This approach allows us to systematically identify not only the optimal number of MPP layers that balances performance and cost, but also the optimal configuration of each layer's parameters.

This new algorithm integrated with further treatment mentioned above is referred to as Alternating MOPSO

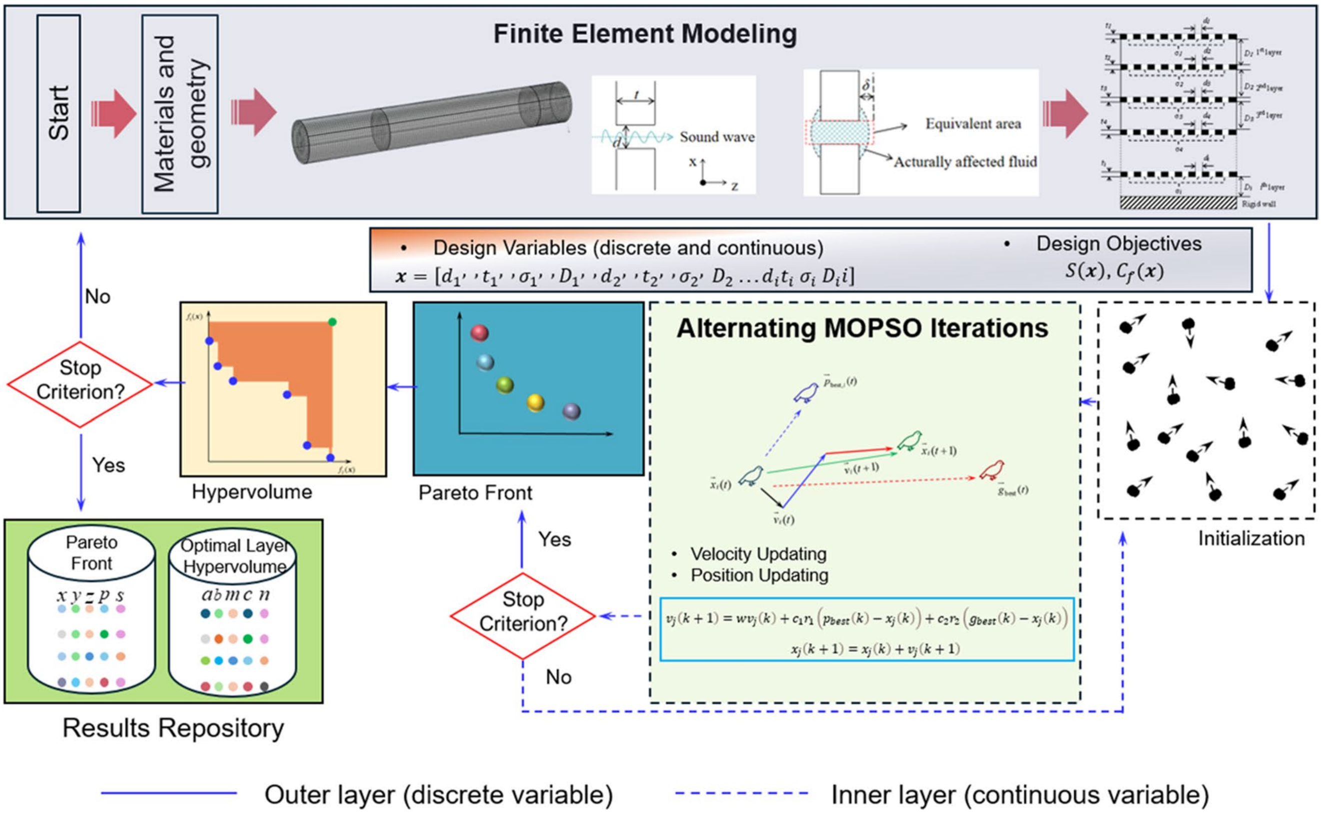

**Fig. 10** Integrated framework for MPP design optimization

in this study. It is developed using in-house code, and its implementation is demonstrated in the following Algorithm. It is worth mentioning that in our alternating optimization framework, particle memories ($p_{\text{best}}$ arrays) are re-initialized at each discrete variable pass to ensure unbiased exploration of each discrete configuration. Only the global repository of non-dominated solutions accumulates across different discrete scenarios, as detailed in Algorithm line 7.

Algorithm: Alternating MOPSO

```
1  Initialize problem parameters: define cost function, set variable bounds
2  Set MOPSO parameters: maximum number of iterations, number of populations, coefficients for MOPSO
3  Alternating optimization loop:
4  For global _it = 1 to MaxGlobalIt:
5      For discrete _var = 1 to 3:
6          -Set n _var based on discrete _var
7          -Initialize population (random positions, velocities, constraints)
8          -Evaluate particles and update personal bests
9          -Determine non-dominated particles (add to repository)
10         For it = 1 to MaxIt:
11             For each particle:
12                 -Select leader from repository
13                 -Update velocity and position
14                 -Apply constraints
15                 -Recalculate costs
16                 -Apply mutation with probability
17                 -Update personal best if dominated
18             End For
19             -Add non-dominated particles to repository
20             -Remove dominated particles and maintain repository size
21         End For
22         -Calculate hypervolume and track best results
23     End For
24 End For
25 Output best results (discrete variable, hypervolume, Pareto front)
```

With the proposed optimization algorithm and well-validated FE model, the integrated design framework can be established to carry out the inverse optimization analysis, as depicted in Fig. 10. The solid line represents the outer layer, where the algorithm iterates over different discrete variable values corresponding to the number of layers. It is worth mentioning that the optimization algorithm is developed in *MATLAB*, while the FE simulation is conducted using *COMSOL Multiphysics*. Hence, performing autonomous optimization analysis necessitates the seamless integration of these development environments. Specifically, we develop a script to build the interface between these two environments. The interface allows the FE simulation to be activated and carried out backstage without manual graphical user interface (GUI) operation, and the analysis results to be exported to the algorithm for design objective assessment and subsequent sampling guidance. Through the automatic and iterative analysis during the design optimization process, the final non-dominated solutions can be identified under multi-objective optimization framework.

## Results and Discussion

The inverse optimization analysis using the proposed Alternating MOPSO algorithm is conducted on a personal computer equipped with an i5-8400 CPU, 4 GB of RAM, and the Windows 10 Home operating system. As mentioned, a single FE simulation run takes approximately 2 min. The operational parameters, as outlined in the pseudo code in Sect. 3.2, are set to 4 for maximum number of iterations (denoted as *MaxIt* in the pseudo code), 2 for maximum number of global iterations (denoted as *MaxGlobalIt* in the pseudo code), 20 for number of populations, 2 for coefficients for MOPSO implementation. This setup is expected to ensure satisfactory optimization convergence with a tractable computational cost of approximately 20 h. Therefore, no surrogate model is needed to replace the FE model, in order to ensure the high prediction accuracy that has already been validated in Sect. 2.2.

The Pareto solutions from the analysis are listed in Table 1, and their corresponding Pareto fronts are illustrated in Fig. 11. The performance measure, represented on the vertical axis, employs the negative $S(\boldsymbol{x})$ to adhere to the minimization problem. Totally, the nineteen solutions exist in the Pareto solution set, including the optimized MPPs with different layers. Although the MPPs with single layer are generally inferior in terms of the performance (denoted by $S$) compared to multi-layer MPPs, they incur less fabrication costs (denoted by $C_f$). However, within the single-layer MPPs, some solutions, such as Solution No. 1 and No. 2, still exhibit notable cost due to the decreasing diameters of the holes, consistent with the cost definition in Eq. (21). While reducing the hole diameter appears to enhance the performance, such strategy may not be cost effective as the hole perforation plays a major role in cost, as can be seen from Eq. (21). By fitting the solution points with a smooth curve, the derivative (i.e., slope) of this curve quantitatively represents the sensitivity of the acoustic performance with respect to cost. The characteristic knee point emerges where the curve's slope decreases substantially, marking the threshold beyond which additional cost investment provides progressively smaller acoustic performance gains. This point identifies the region of diminishing returns where cost effectiveness begins to decline.

**Table 1** Optimized geometric parameters in Pareto solutions (*d* and *t* are in millimeters, $\sigma$ is in percentage, *D* is in centimeter, and $C_f$ is in HKD)

| Solution No. | $d_1$ | $t_1$ | $\sigma_1$ | $D_1$ | $d_2$ | $t_2$ | $\sigma_2$ | $D_2$ | $d_3$ | $t_3$ | $\sigma_3$ | $D_3$ | $C_f$ | -S |
|---|---|---|---|---|---|---|---|---|---|---|---|---|---|---|
| 1 | 0.29 | 0.20 | 0.89 | 6.78 | - | - | - | - | - | - | - | - | 5381.41 | −49.90 |
| 2 | 0.26 | 0.16 | 0.44 | 5.64 | - | - | - | - | - | - | - | - | 3225.95 | −48.22 |
| 3 | 0.34 | 0.10 | 0.58 | 7.56 | - | - | - | - | - | - | - | - | 2628.83 | −45.46 |
| 4 | 0.30 | 0.23 | 0.37 | 7.50 | - | - | - | - | - | - | - | - | 2118.08 | −40.45 |
| 5 | 0.47 | 0.24 | 0.84 | 6.29 | - | - | - | - | - | - | - | - | 1990.96 | −37.97 |
| 6 | 0.50 | 0.24 | 0.61 | 6.23 | - | - | - | - | - | - | - | - | 1269.95 | −35.90 |
| **7** | 0.41 | 0.10 | 0.26 | 3.04 | - | - | - | - | - | - | - | - | 788.02 | −35.47 |
| 8 | 0.61 | 0.42 | 0.46 | 5.02 | - | - | - | - | - | - | - | - | 661.61 | −28.32 |
| 9 | 0.79 | 0.10 | 0.69 | 3.80 | - | - | - | - | - | - | - | - | 568.75 | −28.02 |
| 10 | 0.74 | 0.23 | 0.38 | 5.76 | - | - | - | - | - | - | - | - | 372.08 | −24.42 |
| 11 | 0.66 | 0.10 | 0.20 | 6.52 | - | - | - | - | - | - | - | - | 238.74 | −21.68 |
| 12 | 0.62 | 0.58 | 1.54 | 5.89 | 1.00 | 0.44 | 0.58 | 3.11 | - | - | - | - | 2382.77 | −42.91 |
| 13 | 0.57 | 0.62 | 1.09 | 4.53 | 1.00 | 0.10 | 0.79 | 4.47 | - | - | - | - | 2141.24 | −42.53 |
| 14 | 0.74 | 0.79 | 0.98 | 3.45 | 0.91 | 0.31 | 0.59 | 2.46 | - | - | - | - | 1318.41 | −37.17 |
| 15 | 0.38 | 0.49 | 2.00 | 3.21 | 0.24 | 0.54 | 1.14 | 3.02 | 0.76 | 0.19 | 0.50 | 2.78 | 17926.46 | −62.28 |
| 16 | 0.44 | 0.46 | 1.79 | 3.32 | 0.27 | 0.36 | 1.03 | 2.66 | 0.66 | 0.17 | 0.48 | 2.58 | 12604.88 | −60.24 |
| 17 | 0.63 | 0.27 | 1.10 | 2.70 | 0.20 | 0.16 | 0.33 | 2.15 | 1.00 | 0.10 | 0.20 | 1.19 | 5713.94 | −57.36 |
| 18 | 0.63 | 0.31 | 1.16 | 3.92 | 0.20 | 0.29 | 0.29 | 3.13 | 0.51 | 0.10 | 0.20 | 1.45 | 5565.67 | −53.34 |
| 19 | 0.94 | 0.96 | 1.60 | 2.03 | 0.29 | 0.82 | 0.49 | 0.10 | 0.67 | 0.86 | 0.84 | 1.33 | 5001.29 | −49.24 |

Note: Red color denotes the solutions for discussions

**Fig. 11** Pareto front corresponding to Pareto solution set

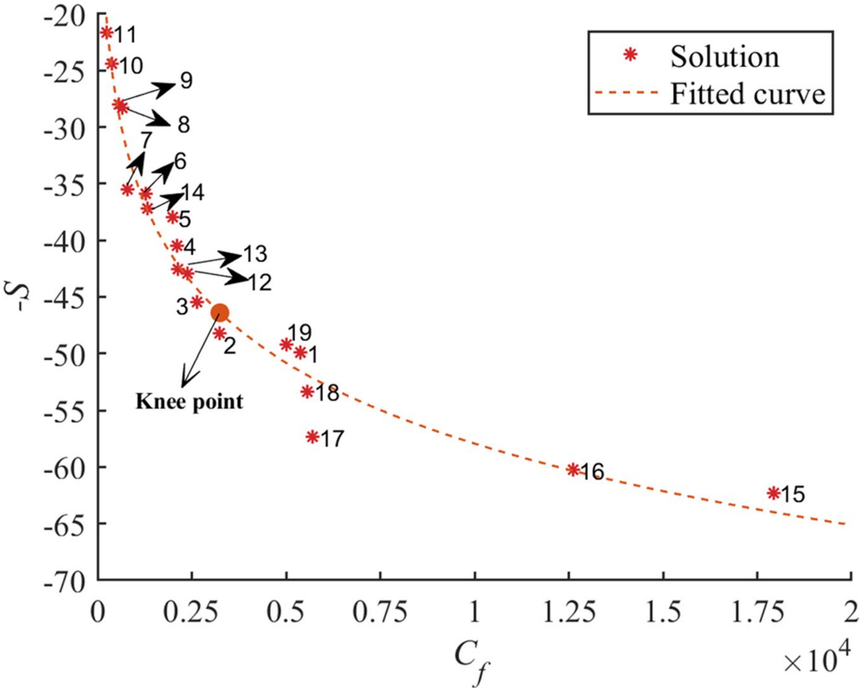

As the number of layers in the MPP increases, the complexity of fabrication and synthesis also rises, leading to higher cost. However, this cost increase is accompanied by a significant improvement in performance. For example, the top-performing 3-layer MPP (Solution No. 15) surpasses the single-layer MPP (Solution No. 1) by 13 units. Moreover, 3-layer MPP solutions appear more cost-effective, as their enhanced performance is achieved through the combinatory design of more geometric parameters rather than by mainly decreasing hole diameters. 2-layer MPP solutions fall in between. Although the multi-objective optimization framework does not directly incorporate objective function weights (Eq. (22)), the resulting Pareto solution set can be subsequently filtered according to engineering priorities and application-specific requirements. This approach effectively introduces "virtual weighting" through post-optimization selection. For noise-sensitive applications, engineers may prioritize solutions with superior acoustic performance, while cost-constrained scenarios may warrant selection of more economical alternatives from the solution set. Compared to the direct aggregation of weighted design objectives in single-objective optimization, the multi-objective optimization substantially reduces the risk of local optima convergence.

We also conduct an in-depth performance examination, as performance is implicitly governed by geometric parameters (as shown in Eq. (17)), using the FE analysis outlined in Sect. 2.1. Specifically, we select two solutions with the highest and lowest performance, i.e., Solution No. 1 and No. 11 (highlighted red in Table 1), for single-layer MPPs. Their performance varies significantly, which is consistent with the respective SAC curves shown in Fig. 12a. We further examine the peak SAC value of Solution No. 1 at 720 Hz by analyzing its sound pressure distribution in the tube, as illustrated in Fig. 12a. For comparison, the sound pressure distribution of Solution No. 11 at the same frequency is also included. In Solution No. 11, insufficient sound absorption capacity leads to sound wave reflection in the waveguide subdomain, increasing the intensity of the incident sound wave (shown in dark red). Similarly, we select two solutions, Solution No. 15 and No. 19 (highlighted red in Table 1), for 3-layer MPPs for comparison. Enhanced performance is clearly observed compared to the single-layer MPP solutions. Although Solution No. 15 performs better than Solution No. 19, the difference is not as pronounced as in the two single-layer MPP solutions. This indicates the relatively robust performance of multi-layer MPPs when properly designed. The comparison of sound pressure distributions at 480 Hz for these two solutions also explains the fundamental cause behind the observation.

The current Pareto solution set comprises eleven single-layer MPP solutions, three 2-layer MPP solutions, and five 3-layer MPP solutions. Such a distribution of solutions implies that further increasing the layers of MPP may not be very feasible when considering the balance between performance and cost. This Pareto solution set, derived from a multi-objective optimization framework, demonstrates

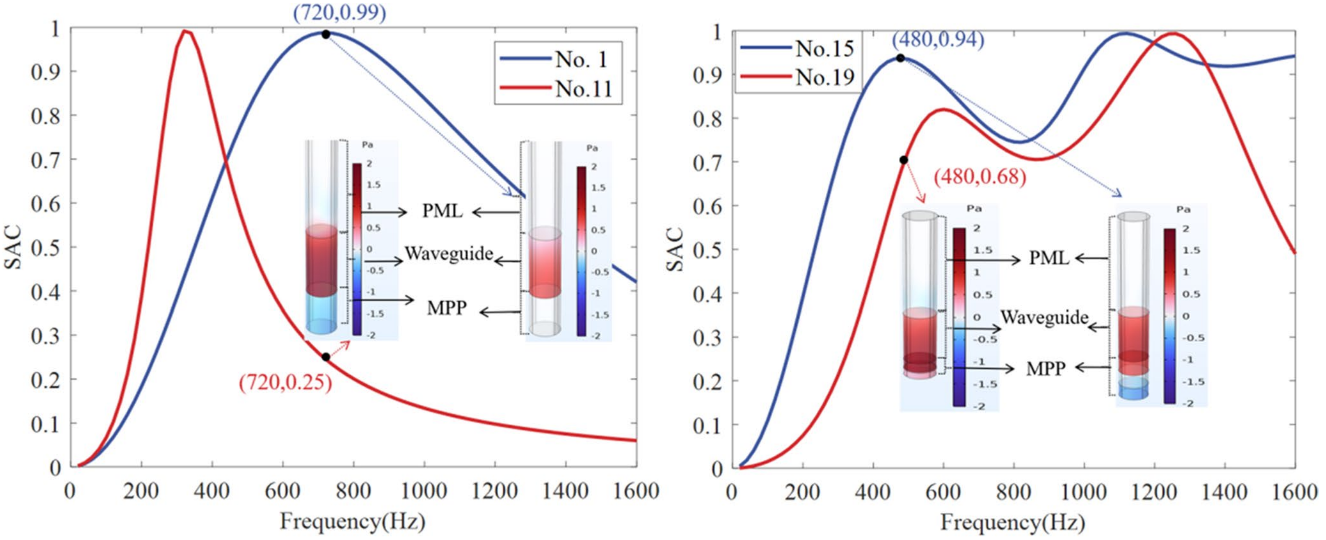

(a) (b)

**Fig. 12** The comparison of SAC curves and sound pressure distributions at specific frequencies: (**a**) Sing-layer MPP solutions; (**b**) 3-layer MPP solutions

increased flexibility in practical operations compared to a single solution from a single-objective optimization framework. With multiple choices available, engineers can integrate their preferences and judgment to select the best solution for a specific application context. For example, if performance is the top priority, increasing the number of layers at the expense of higher costs is worthwhile. Additionally, more objective methods, such as post-filtering and recommendation systems, can aid in achieving wise decision-making.

Due to the stochastic nature of optimization, we conduct two additional optimization runs to elucidate the interrelation among optimized solutions in this design problem. In particular, we obtain twenty-one and seventeen non-dominated solutions from the second and third runs, respectively. We gather solutions from all three runs and perform a dominance analysis, resulting in a new Pareto solution set and respective Pareto front, as shown in Table 2; Fig. 13. This solution set includes a total of twenty-eight solutions, more than those identified in each individual run. While there is no closed-form approach to determine the exact number of solutions, more iterations in the optimization analysis can generally yield an increasing number of solutions in a high-dimensional design space. Among the solutions, Solution No. 26 and No. 28 (highlighted red in Table 2) appear to be optimal candidates, considering the tradeoff between cost and performance. As shown in Fig. 13, cost increase is accompanied by a significant performance improvement until Solution No. 26. Such phenomenon proves that further increasing the layers of MPP may not be very feasible. Overall, this new solution set from the three runs exhibits similar characteristics to the ones in Table 1, though individual differences may exist. The corresponding fitted curve reveals a knee point position that closely aligns with the one shown in Fig. 11. These consistencies confirm the convergence of the optimization analysis and validate the robustness and effectiveness of the proposed methodology for MPP design.

## Conclusion

The low-frequency components of indoor noise in buildings significantly degrade residential quality. Although MPPs have been proven effective in mitigating low-frequency noise, their size, fabrication process, and associated costs need to be considered during development to ensure practical viability. In this paper, we focus on designing MPPs to optimize both sound absorption performance and fabrication cost through an integrated design framework. A FE model of the MPP is established and validated using impedance tube tests to accurately predict the SAC of MPPs under different operating conditions. A novel MOPSO algorithm is then developed to conduct inverse analysis-based design, utilizing the above well-established MPP FE model. This algorithm can effectively address the technical challenges arising from the nature of the design problem, which involves both discrete and continuous design variables with

**Table 2** Optimized geometric parameters in Pareto solutions for three runs (*d* and *t* are in millimeters, $\sigma$ is in percentage, *D* is in centimeter, and $C_f$ is in HKD)

| Solution No. | $d_1$ | $t_1$ | $\sigma_1$ | $D_1$ | $d_2$ | $t_2$ | $\sigma_2$ | $D_2$ | $d_3$ | $t_3$ | $\sigma_3$ | $D_3$ | $C_f$ | -S |
|---|---|---|---|---|---|---|---|---|---|---|---|---|---|---|
| 1 | 0.34 | 0.10 | 0.58 | 7.56 | - | - | - | - | - | - | - | - | 2628.83 | −45.46 |
| 2 | 0.39 | 0.10 | 0.27 | 4.41 | - | - | - | - | - | - | - | - | 929.29 | −37.30 |
| 3 | 0.67 | 0.10 | 0.51 | 2.53 | - | - | - | - | - | - | - | - | 588.58 | −31.61 |
| 4 | 0.79 | 0.10 | 0.69 | 3.80 | - | - | - | - | - | - | - | - | 568.75 | −28.02 |
| 5 | 0.72 | 0.41 | 0.49 | 2.13 | - | - | - | - | - | - | - | - | 512.78 | −27.52 |
| 6 | 0.93 | 0.10 | 0.70 | 3.81 | - | - | - | - | - | - | - | - | 414.80 | −24.74 |
| 7 | 0.86 | 0.33 | 0.47 | 2.29 | - | - | - | - | - | - | - | - | 343.24 | −24.42 |
| 8 | 0.97 | 0.10 | 0.57 | 3.45 | - | - | - | - | - | - | - | - | 312.29 | −23.74 |
| 9 | 0.95 | 0.11 | 0.51 | 3.29 | - | - | - | - | - | - | - | - | 292.94 | −23.71 |
| 10 | 0.66 | 0.10 | 0.20 | 6.52 | - | - | - | - | - | - | - | - | 238.74 | −21.68 |
| 11 | 1.00 | 0.30 | 0.39 | 5.66 | - | - | - | - | - | - | - | - | 215.36 | −18.55 |
| 12 | 0.77 | 0.12 | 0.20 | 7.94 | - | - | - | - | - | - | - | - | 179.26 | −18.39 |
| 13 | 0.91 | 0.33 | 0.20 | 0.30 | - | - | - | - | - | - | - | - | 140.52 | −15.22 |
| 14 | 1.00 | 0.44 | 0.20 | 6.20 | - | - | - | - | - | - | - | - | 125.88 | −12.67 |
| 15 | 0.43 | 0.51 | 1.42 | 2.89 | 0.26 | 0.75 | 1.14 | 4.59 | - | - | - | - | 12812.42 | −61.16 |
| 16 | 0.45 | 0.45 | 1.36 | 2.63 | 0.25 | 0.96 | 1.11 | 4.53 | - | - | - | - | 12619.62 | −60.92 |
| 17 | 0.43 | 0.11 | 0.64 | 3.68 | 0.71 | 0.76 | 0.81 | 1.39 | - | - | - | - | 2648.09 | −49.35 |
| 18 | 1.00 | 0.54 | 1.29 | 3.02 | 0.64 | 0.88 | 0.63 | 5.50 | - | - | - | - | 1531.41 | −44.89 |
| 19 | 0.78 | 0.25 | 1.08 | 2.85 | 1.00 | 0.46 | 0.59 | 3.36 | - | - | - | - | 1246.90 | −42.00 |
| 20 | 1.00 | 0.22 | 0.73 | 2.40 | 1.00 | 0.56 | 0.38 | 3.34 | - | - | - | - | 605.54 | −37.10 |
| 21 | 0.38 | 0.49 | 2.00 | 3.21 | 0.24 | 0.54 | 1.14 | 3.02 | 0.76 | 0.19 | 0.50 | 2.78 | 17926.46 | −62.28 |
| 22 | 0.59 | 0.30 | 1.77 | 3.46 | 0.54 | 0.74 | 0.75 | 2.35 | 0.20 | 0.62 | 0.95 | 3.19 | 16028.90 | −62.13 |
| 23 | 0.66 | 0.30 | 1.76 | 3.95 | 0.59 | 0.74 | 0.74 | 1.73 | 0.20 | 0.71 | 0.99 | 3.31 | 15802.67 | −61.68 |
| 24 | 0.44 | 0.46 | 1.79 | 3.32 | 0.27 | 0.36 | 1.03 | 2.66 | 0.66 | 0.17 | 0.48 | 2.58 | 12604.88 | −60.24 |
| 25 | 0.49 | 0.10 | 1.77 | 3.30 | 0.54 | 0.71 | 0.83 | 2.50 | 0.31 | 0.70 | 0.95 | 3.20 | 10338.18 | −58.16 |
| 26 | 0.63 | 0.27 | 1.10 | 2.70 | 0.20 | 0.16 | 0.33 | 2.15 | 1.00 | 0.10 | 0.20 | 1.19 | 5713.94 | −57.36 |
| 27 | 0.63 | 0.31 | 1.16 | 3.92 | 0.20 | 0.29 | 0.29 | 3.13 | 0.51 | 0.10 | 0.20 | 1.45 | 5565.67 | −53.34 |
| 28 | 0.81 | 0.22 | 1.79 | 4.41 | 0.72 | 0.87 | 0.92 | 2.24 | 0.53 | 0.85 | 0.94 | 2.35 | 4088.76 | −52.87 |

Note: Red color denotes the potentially good solutions

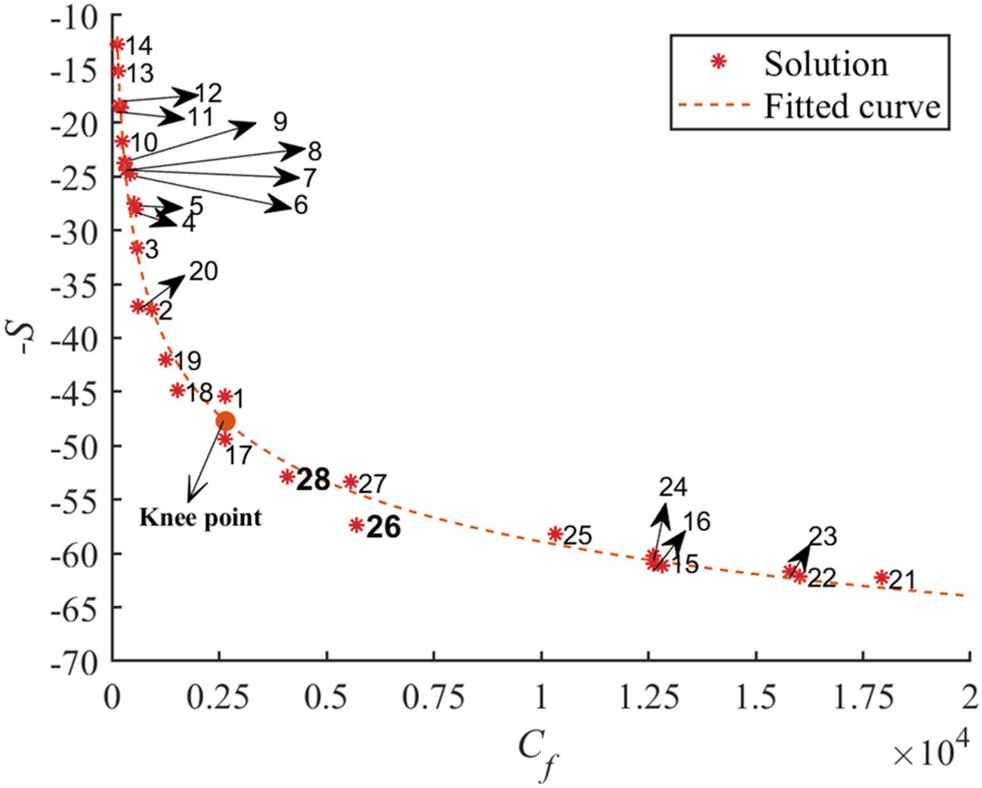

**Fig. 13** Pareto front corresponding to Pareto solution set for three runs

correlations. An in-house code is developed to facilitate the entire design implementation, yielding a set of non-dominated solutions. The results offer useful guidance for decision making, demonstrating the feasibility of the proposed methodology.

In the future, additional experimental validation encompassing diverse MPP configurations will be conducted to ensure the accuracy and reliability of the numerical model in capturing these intricate physical interactions. The post-filtering and recommendation systems can be established for allowing architects and builders to select configurations based on project-specific acoustic and budgetary requirements. To account for vibration valley effects, we plan to investigate flexible panel implementations in MPP designs. This advancement will require careful consideration of structural-acoustic coupling phenomena, which significantly increases computational complexity. Consequently, parallel development of efficient numerical strategies will be essential to make such analyses computationally tractable. Moreover, various design objectives regarding performance and cost can be formulated. For example, instead of examining the sound absorption capacity over the entire frequency range, we can set multiple objectives to assess the capacity at different sub-frequency ranges defined by the users. For practical deployment, a more comprehensive cost model would be crucial. The proposed approach ensures a tailored design purpose. More efforts will be made to further advance optimization algorithms to handle more complex and general design problems of MPPs and other sound absorption materials. On the environmental front, the carbon footprint per square metre of MPP could be compared with baseline porous foams in our future work.

**Acknowledgements** The research is supported part by the start-up fund provided by The Hong Kong Polytechnical University (PolyU), and part by the research project fund from Research Institute for Sustainable Urban Development (RISUD) at PolyU.

**Funding** Open access funding provided by The Hong Kong Polytechnic University

## Declarations

**Conflict of interest** On behalf of all authors, the corresponding author states that there is no conflict of interest.

## References

1. Sheng DDCV et al (2024) Potential of wood fiber/polylactic acid composite microperforated panel for sound absorption application in indoor environment. Constr Build Mater 444:137750
2. Wang H, Gao H, Cai M (2019) Simulation of traffic noise both indoors and outdoors based on an integrated geometric acoustics method. Build Environ 160:106201
3. Li Q et al (2024) Development of a low-frequency broadband sound absorber based on a micro-perforated panel coupled with the Helmholtz resonator system. Phys Scr 99(8):085902
4. Sun W et al (2024) Low-frequency ultra-broadband absorbers with conical cavity-coupled porous materials. Appl Acoust 221:110035
5. Ye X et al (2024) Modeling of the hysteretic behavior of nonlinear particle damping by fourier neural network with transfer learning. Mech Syst Signal Process 208:111006
6. Allard J, Atalla N (2009) Propagation of sound in porous media: modelling sound absorbing materials. Wiley
7. Min H, Lou H, Zhao Y (2024) Acoustic properties of a micro-perforated muffler with parallel-arranged cavities of different depths. Build Environ. https://doi.org/10.1016/j.buildenv.2024.111728
8. Larsson M et al (2009) A module based active noise control system for ventilation systems, part II: performance evaluation. Int J Acoust Vib 14(4):196–206
9. Mak CM et al (2015) Sustainable noise control system design for building ventilation systems. Indoor Built Environ 24(1):128–137
10. Abo-Qudais S, Abu-Qdais H (2005) Perceptions and attitudes of individuals exposed to traffic noise in working places. Build Environ 40(6):778–787
11. Douglas O, Murphy E (2016) Source-based subjective responses to sleep disturbance from transportation noise. Environ Int 92:450–456
12. Christensen JS et al (2017) Exposure to residential road traffic noise prior to conception and time to pregnancy. Environ Int 106:48–52
13. Pitchika A et al (2017) Long-term associations of modeled and self-reported measures of exposure to air pollution and noise at residence on prevalent hypertension and blood pressure. Sci Total Environ 593:337–346
14. Tabraiz S et al (2015) Study of physio-psychological effects on traffic wardens due to traffic noise pollution; exposure-effect relation. J Environ Health Sci Eng 13:1–8
15. Zhao X, Yu Y, Wu Y (2016) Improving low-frequency sound absorption of micro-perforated panel absorbers by using mechanical impedance plate combined with Helmholtz resonators. Appl Acoust 114:92–98
16. Rochat JL, Reiter D (2016) Highway traffic noise. Acoust Today 12(4):38
17. Cao L et al (2018) Porous materials for sound absorption. Compos Commun 10:25–35
18. Sahu NR, Mandal BB (2024) Development of tunable acoustic materials with inline cavity structure for enhanced sound absorption and transmission loss. J Build Eng 82:108305
19. Wang Z et al (2022) Study on sound absorption model of porous asphalt concrete based on three-dimensional morphology of air voids. Constr Build Mater 338:127537
20. Zhang B et al (2018) Locally resonant meta-composite for soundproof of building envelops: analytical model and experiment. Constr Build Mater 164:792–798
21. Lv L (2015) Effect of micro-slit plate structure on the sound absorption properties of discarded corn cob husk fiber. Fibers Polym 16:1562–1567
22. Yang Z et al (2010) Acoustic metamaterial panels for sound attenuation in the 50–1000 hz regime. Appl Phys Lett. https://doi.org/10.1063/1.3299007
23. Xu Q (2021) A tunable massless membrane metamaterial for perfect and low-frequency sound absorption. J Sound Vib 493:115823
24. Toyoda M, Mu RL, Takahashi D (2010) Relationship between Helmholtz-resonance absorption and panel-type absorption in finite flexible microperforated-panel absorbers. Appl Acoust 71(4):315–320
25. Sakagami K, Morimoto M, Yairi M (2009) A note on the relationship between the sound absorption by microperforated panels and panel/membrane-type absorbers. Appl Acoust 70(8):1131–1136
26. Maa D (1998) Potential of microperforated panel absorber. J Acoust Soc Am 104(5):2861–2866
27. Dah-You M (1997) General theory and design of microperforated-panel absorbers. Acta Acustica
28. Rezaieyan E et al (2024) Acoustic properties of natural fiber reinforced composite micro-perforated panel (NFRC-MPP) made from Cork fiber and polylactic acid (PLA) using 3D printing. J Build Eng 84:108491
29. Bokhove J, Schuur B, De Haan AB (2013) Resin screening for the removal of pyridine-derivatives from waste-water by solvent impregnated resin technology. React Funct Polym 73(3):595–605
30. Chin V, Sheng DD, Yahya MNB (2022) Che din, sound absorption of microperforated panel made from coconut fiber and polylactic acid composite. J Nat Fibers 19(7):2719–2729
31. Hoshi K (2020) Implementation experiment of a honeycomb-backed MPP sound absorber in a meeting room. Appl Acoust 157:107000
32. Bravo T, Maury C, Pinhède C (2012) Vibroacoustic properties of thin micro-perforated panel absorbers. J Acoust Soc Am 132(2):789–798
33. Dong B et al (2023) Flow effects of microperforated-panel casing treatments in a contra-rotating fan. Int J Mech Sci 239:107879
34. Li C et al (2023) Noise reduction in helicopter cabins using microperforated panel composite sound absorption structures. Appl Sci 13(14):8153
35. Cobo P, Ruiz H, Alvarez J (2010) Double-layer microperforated panel/porous absorber as liner for anechoic closing of the test section in wind tunnels. Acta Acustica united with Acustica 96(5):914–922
36. Wu H (2025) An integrated SEA-deep learning approach for the optimal geometry performance of noise barrier. Machines 13(8):670
37. Yafei S et al (2003) Experimental research of noise control in the fighter cockpit using microperforated panel absorber structure. ACTA ACUSTICA 28(4):294–298
38. Chu J et al (2023) A Multi-Layer Micro-Perforated Panel Structure Based on Curled Space for Broadband Sound Absorption at Low Frequencies. Available at SSRN 4289209
39. Kong W, Fu T (2024) A novel butterfly double-panel metastructure filled with porous materials for broadband low-frequency sound absorption. J Build Eng 97:110935

40. Cingolani M et al (2021) A trial acoustic improvement in a lecture hall with MPP sound absorbers and FDTD acoustic simulations. Appl Sci 11(6):2445
41. Sakagami K et al (2021) Application of transparent microperforated panels to acrylic partitions for desktop use: A case study by prototyping. UCL Open Environ, 3
42. Wang G (2023) Investigation on low frequency acoustic characteristics of parallel-arranged microperforated panel with aerogel-filled back cavities. Appl Acoust 207:109347
43. Xiang L et al (2024) Optimization of hybrid microperforated panel and nonuniform space-coiling channels for broadband low-frequency acoustic absorption. Appl Acoust 216:109763
44. Bravo T, Maury C (2021) Vibrational effects on the optimization of micro-perforated partitions based on a causality criterion. in Proceedings of Meetings on Acoustics. : AIP Publishing
45. Bravo T, Maury C, Pinhède C (2014) Optimising the absorption and transmission properties of aircraft microperforated panels. Appl Acoust 79:47–57
46. Fuchs HV, Zha X (2006) Micro-perforated structures as sound absorbers–a review and outlook. Acta acustica united with acustica 92(1):139–146
47. Drotleff H, Zhou X (2001) Attractive room acoustic design for multi-purpose halls. Acta Acust United Acust 87(4):500–504
48. Herrin D, Liu J, Seybert A (2011) Properties and applications of microperforated panels. Sound Vib 45(7):6–9
49. Li Z, Wang L, Gu K (2024) Efficient reliability-based concurrent topology optimization method under PID-driven sequential decoupling framework. Thin-Walled Struct 203:112117
50. Liu J, Wang L, Wu Z (2024) Novel study on active reliable PID controller design based on probability density evolution method and interval-oriented sequential optimization strategy. Comput Methods Appl Mech Eng 427:117057
51. Cobo P et al (2019) A wideband triple-layer microperforated panel sound absorber. Compos Struct 226:111226
52. Qian YJ et al (2014) Optimization of multi-size micro-perforated panel absorbers using multi-population genetic algorithm. Noise Control Eng J 62(1):37–46
53. Lu C et al (2018) Comparison analysis and optimization of composite micro-perforated absorbers in sound absorption bandwidth. Acoust Aust 46:305–315
54. Wang J, Bennett GJ (2023) Multi-chamber micro-perforated panel absorbers optimised for high amplitude broadband absorption using a two-point impedance method. J Sound Vib 547:117527
55. Zhao L, Lin TR (2022) A turned double-layer microperforated panel for low frequency sound absorption in enclosures with limited cavity space. Appl Acoust 188:108594
56. Ao WK, Reynolds P (2019) Evaluation of eddy current damper for vibration control of a frame structure. J Phys Commun 3(5):055013
57. Hashemi Z et al (2024) Optimization and comparative analysis of micro-perforated panel sound absorbers: a study on structures and performance enhancement. Measurement 236:115123
58. Li H (2023) Development of ultra-broadband sound absorber based on double-layered irregular honeycomb microperforated panel. Phys Scr 98(7):075015
59. Sheng H et al (2024) Quasi-periodic sonic black hole with low-frequency acoustic and elastic bandgaps. Compos Struct 337:118046
60. Jian L et al Multifunctional Tpms-Based Metastructures With Enhanced Low-Frequency Sound Absorption and High Bending Stiffness Performance. Available at SSRN 5109242
61. Stinson MR, Shaw E (1985) Acoustic impedance of small, circular orifices in thin plates. J Acoust Soc Am 77(6):2039–2042
62. Ruiz H, Cobo P (2011) Proposal of alternative designs for microperforated panels. in INTER-NOISE and NOISE-CON Congress and Conference Proceedings. : Institute of Noise Control Engineering
63. Carbajo J (2015) A finite element model of perforated panel absorbers including viscothermal effects. Appl Acoust 90:1–8
64. Deacon M, Series D et al (2018) 80(3): 141–152
65. Gerdes R, Alexander J, Herdtle T (2013) Acoustic performance prediction of Micro-Perforated panels using computational fluid dynamics and finite element analysis. SAE Technical Paper.
66. Sakagami K (2008) A pilot study on improving the absorptivity of a thick microperforated panel absorber. Appl Acoust 69(2):179–182
67. Chin D, Bin Yahya (2023) Bin Che Din, microperforated panel made by biodegradable natural fiber composite for acoustic application. Structural integrity and monitoring for composite materials. Springer, pp 61–71
68. Buildings Department HKSAR, China (2015) Code of practice for fire safety in buildings
69. Committee S (2019) EN 13501-1: Fire classification of construction products andbuilding elements-Part 1: Classification using test data from reaction tofire tests
70. Zaporozhets O (2022) Indoor noise A-level assessment related to the environmental noise spectrum on the building facade. Appl Acoust 185:108380
71. Ao WK (2024) Tracking long-term modal behaviour of a footbridge and identifying potential SHM approaches. J Civil Struct Health Monit 14(5):1311–1337
72. Liu Y, Wang L, Ng BF (2025) Multitask-transfer-learning method for random-force frequency identification considering multisource uncertainties. AIAA J 63(6):2345–2360
73. Koch C (2002) Determination of the acoustic output of a harmonic scalpel. IEEE Trans Ultrason Ferroelectr Freq Control 49(11):1522–1529
74. Zhu J et al (2023) Multilayer structures for high-intensity sound energy absorption in low-frequency range. Int J Mech Sci 247:108197
75. Wang C, Liu X (2020) Investigation of the acoustic properties of corrugated micro-perforated panel backed by a rigid wall. Mech Syst Signal Process 140:106699
76. Lee YY, Lee E, Ng CF (2005) Sound absorption of a finite flexible micro-perforated panel backed by an air cavity. J Sound Vib 287(1–2):227–243
77. Wang C, Huang L (2011) On the acoustic properties of parallel arrangement of multiple micro-perforated panel absorbers with different cavity depths. J Acoust Soc Am 130(1):208–218
78. Zhang D et al (2025) A convolutional neural network driven suspension control strategy to enhance sustainability of high-speed trains. Energy Conversion and Management: X. https://doi.org/10.1016/j.ecmx.2025.101183
79. Zhang D et al (2024) Improving the energy efficiency and riding comfort of high-speed trains across slopes by the optimized suspension control. Energy 307:132660
80. Kennedy J, Eberhart R (1995) Particle swarm optimization. in Proceedings of ICNN'95-international conference on neural networks. : ieee
81. Zhang Y, Zhou K, Tang J (2024) Harnessing collaborative learning automata to guide multi-objective optimization based inverse analysis for structural damage identification. Appl Soft Comput 160:111697
82. Zhang Y, Zhou K, Tang J (2024) Piezoelectric impedance-based high-accuracy damage identification using sparsity conscious multi-objective optimization inverse analysis. Mech Syst Signal Process 209:111093

83. Wang L et al (2024) Multi-source uncertainty-oriented dynamic force reconstruction framework based on adaptive fitting precise integration and optimized wavelet denoising. Struct Multidiscip Optim 67(3):28
84. Guerreiro AP, Fonseca CM, Paquete L (2021) The hypervolume indicator: computational problems and algorithms. ACM Comput Surv 54(6):1–42